

Deep Image Mining for Diabetic Retinopathy Screening

Gwenolé Quéllec^{a,*}, Katia Charrière^{b,a}, Yassine Boudi^{b,a}, Béatrice Cochener^{c,a,d}, Mathieu Lamard^{c,a}

^aInserm, UMR 1101, Brest, F-29200 France

^bInstitut Mines-Telecom; Telecom Bretagne, Dpt ITI, Brest, F-29200 France

^cUniv Bretagne Occidentale, Brest, F-29200 France

^dService d'Ophthalmologie, CHRU Brest, Brest, F-29200 France

Abstract

Deep learning is quickly becoming the leading methodology for medical image analysis. Given a large medical archive, where each image is associated with a diagnosis, efficient pathology detectors or classifiers can be trained with virtually no expert knowledge about the target pathologies. However, deep learning algorithms, including the popular ConvNets, are black boxes: little is known about the local patterns analyzed by ConvNets to make a decision at the image level. A solution is proposed in this paper to create heatmaps showing which pixels in images play a role in the image-level predictions. In other words, a ConvNet trained for image-level classification can be used to detect lesions as well. A generalization of the backpropagation method is proposed in order to train ConvNets that produce high-quality heatmaps. The proposed solution is applied to diabetic retinopathy (DR) screening in a dataset of almost 90,000 fundus photographs from the 2015 Kaggle Diabetic Retinopathy competition. For the task of detecting referable DR, the proposed system outperforms state-of-the-art methods based on deep learning: $A_z = 0.954$, as opposed to $A_z = 0.946$ for Colas et al. (2016) in particular. Performance at the pixel level was evaluated in the DiaretDB1 dataset, where four types of lesions are manually segmented: microaneurysms, hemorrhages, exudates and cotton-wool spots. For all lesion types, the proposed detector, trained with image-level supervision, outperforms recent algorithms, even though they were trained with pixel-level supervision. This detector is part of the RetinOpTIC[®] system for mobile eye pathology screening. Because it does not rely on expert knowledge or manual segmentation for detecting relevant patterns, the proposed solution can potentially discover new biomarkers in images, which makes it a promising image mining tool.

Keywords: deep learning, image mining, pathology screening, lesion detection, diabetic retinopathy

1. Introduction

Retinal pathologies are responsible for millions of blindness cases worldwide. The leading causes of blindness are glaucoma (4.5 million cases), age-related macular degeneration (3.5 million cases) and diabetic retinopathy (2 million cases).¹ Early diagnosis is the key to slowing down the progression of these diseases and therefore preventing the occurrence of blindness. In order to reduce the workload of human interpretation, and therefore streamline retinal pathology screening, various image analysis algorithms have been developed over the last few decades. The first solutions were trained to detect lesions (at the pixel level) using manual segmentations (at the pixel level) for supervision (Winder et al., 2009; Abràmoff et al., 2010): this is what we call computer-aided detection (CADE) algorithms. Based on the detected lesions, other algorithms were trained to detect pathologies (at the image level) (Abràmoff et al., 2010): this is what we call computer-aided diagnosis (CADx) algorithms. In recent years, new algorithms were designed to detect pathologies directly, using diagnoses (at the

image level) only for supervision: these algorithms are based on multiple-instance learning (Amores, 2013) or deep learning (LeCun et al., 2015). Because manual segmentations are not needed, such algorithms can be trained in much larger datasets, such as anonymized archives of examination records. The next challenge is to detect lesions using diagnoses only for supervision. Besides access to large training datasets, such an approach would allow discovery of new biomarkers in images, since algorithms are not limited by the subjectivity of manual segmentations. A few multiple-instance learning algorithms, supervised at the image level, can already detect lesions (Melendez et al., 2015; Quéllec et al., 2016b). To push performance at the pixel level further, it would be useful to take advantage of deep learning, which is currently more powerful for predictions at the image level: a solution is proposed in this paper.

In 2015, a machine learning competition was organized with the goal to design an automated system for grading the severity of diabetic retinopathy (DR) in images.² Images were trained and evaluated at the image level in a publicly-available dataset of almost 90,000 images provided by EyePACS (Cuadros and Bresnick, 2009), a free platform for DR screening. The performance criterion was the inter-rater agreement between the automated predictions and the predictions of human readers. As

*LaTIM - Bâtiment 1 - CHRU Morvan - 2, Av. Foch
29609 Brest CEDEX - FRANCE

Tel.: +33 2 98 01 81 29 / Fax: +33 2 98 01 81 24

Email address: gwenole.quellec@inserm.fr (Gwenolé Quéllec)

¹www.who.int/blindness/causes/priority

²<https://www.kaggle.com/c/diabetic-retinopathy-detection>

usual in pattern recognition competitions (Russakovsky et al., 2015), the top-ranking solutions all relied on deep learning. More precisely, they relied on ensembles of ConvNets. The inter-rater agreement achieved by those solutions was clearly at the level of the inter-rater agreement among human readers (Barriga et al., 2014). ConvNets are artificial neural networks where each neuron only processes one portion of the input image (LeCun et al., 2015). The main building-block of ConvNets are convolutional layers. In those layers, the input image is convolved with multiple filters inside a sliding window. After non-linear post-processing, one activation map is obtained per filter. Those activation maps can be further processed by another convolutional layer, or can be nonlinearly down-sampled by a pooling layer. After several convolutional and pooling layers, ConvNets usually end with dense layers, which produce image-level predictions. Knowing that DR diagnosis usually relies on a very limited number of pixels, namely the presence of a few small lesions, we were eager to know why ConvNets, trained at an image level, were relevant for this task. We have already shown the relevance of algorithms supervised at the image level for grading DR (Quellec et al., 2010a,b, 2012b). However, we were not able to reach a satisfactory level of agreement without explicitly modeling the fact that DR diagnosis may be governed by a single image patch, through multiple-instance learning (Quellec et al., 2012a, 2016c). Hence the starting point of this study: can ConvNets precisely pinpoint the few pixels involved in DR diagnosis? In particular, can they detect the smallest lesions? Or do they simply identify pathological regions roughly in images? Of course, precisely pinpointing lesions is not required for decision making at an image level, but it would be useful to document the proposed automatic diagnoses. Clearly, many users would not trust a black box, like a ConvNet (not to mention an ensemble of ConvNets), if their patient’s health and their liability are at stake. In this paper, a criterion is proposed to detect the pixels involved in the image-level predictions of a ConvNet. Additionally, a novel method is proposed to train the ConvNets in such a way that the quality of these detections is maximized. The proposed solution is part of the RetinOpTIC[®] system for eye pathology screening,³ which integrates a mobile non-mydratic retinograph and algorithms for automated or computer-aided diagnosis.

The remaining of this paper is organized as follows. After a short review of the state of the art in section 2, the proposed solution is summarized in section 3. Section 4 describes the main building blocks of ConvNets, so that we can introduce our novel training algorithm in section 5. Section 6 describes the proposed lesion detection criterion. Section 7 presents experiments in two retinal image datasets (Kaggle and DiaretDB1). We end with a discussion and conclusions in section 8.

2. State of the Art

This section reviews the state of the art of deep learning from an application point of view, namely deep learning for reti-

nal image analysis, and from a methodological point of view, namely visualizing what ConvNets are learning.

2.1. Deep Learning for Retinal Image Analysis

Deep learning was recently applied to various tasks related to retinal image analysis. For landmark segmentation and lesion detection, it was applied at a pixel level. For pathology detection, it was applied at an image level.

At a pixel level, a few algorithms were proposed for segmenting retinal vessels (Maji et al., 2015, 2016; Li et al., 2016) and the optic disc (Lim et al., 2015; Srivastava et al., 2015); others were proposed for detecting microaneurysms (Haloi, 2015) and exudates (Prentasac and Loncaric, 2015), two lesions related to DR. First, Maji et al. (2015, 2016) use an ensemble of ConvNets to classify each pixel as ‘part of a vessel’ or ‘not part of a vessel’. Similarly, Lim et al. (2015) use a ConvNet to classify each pixel as ‘part of the optic cup’, ‘part of the optic disc minus the optic cup’ or ‘not part of the optic disc’. Alternatively, Srivastava et al. (2015) use a network composed of (unsupervised) stacked auto-encoders followed by a supervised layer to classify each pixel as ‘part of the optic disc’ or ‘not part of the optic disc’. For lesion detection, Haloi (2015) and Prentasac and Loncaric (2015) use a ConvNet to classify each pixel as ‘part of a target lesion (a microaneurysm or an exudate, respectively)’ or ‘not part of a target lesion’. In those five algorithms, each pixel is classified through the analysis of a squared region centered on the pixel. In contrast, full images are analyzed in Li et al. (2016): stacked auto-encoders trained on ‘fundus photograph’ / ‘vessel segmentation map’ pairs are used to generate vessel probability maps the size of fundus photographs. Those six algorithms require manual segmentations of training images for supervision.

At an image level, algorithms were proposed for detecting glaucoma (Chen et al., 2015a,b) and age-related macular degeneration (AMD) (Burlina et al., 2016). While Lim et al. (2015) detect glaucomatous patients using the standard cup-to-disc ratio, derived from their deep-learning-based segmentations of the optic disc and cup, Chen et al. (2015a,b) directly classify an image as ‘glaucomatous’ or ‘non-glaucomatous’ through the analysis of a large region of interest centered on the optic disc, using one or two ConvNets. To detect AMD, Burlina et al. (2016) use the OverFeat features, derived from a ConvNet trained on the very large, general-purpose ImageNet dataset: these features are used to train a linear support-vector machine (SVM). Finally, Arunkumar and Karthigaikumar (2016) proposed an algorithm for differentiating multiple pathologies: AMD, DR, macular bunker, retinoblastoma, retinal detachment and retinitis pigmentosa. Similarly to the AMD detector, image features are extracted with a ConvNet and a multi-class SVM is used to differentiate the various pathologies.

Finally, Colas et al. (2016) also use deep learning techniques for detecting referable DR: lesions are first detected (at the pixel level) and then DR severity is graded (at the image level).

2.2. Visualizing what ConvNets are Learning

Because ConvNets are black boxes, many solutions have been proposed to visualize what they have learned. The earliest so-

³<http://www.retinoptic.fr/>

lutions consisted in visualizing the trained filters or intermediate activation maps. Given the large number of convolutional units in a ConvNet, it is hard to find out from a visual inspection which pattern each of them is looking for. One way to address this issue is to find which image, inside a large dataset, maximally activates each convolutional units (Girshick et al., 2014) or to generate an artificial image that maximally activates it (Yosinski et al., 2015). Besides understanding the role of each convolutional units, an additional question arises when training ConvNet at the image level: which regions or pixels, inside the image, play a role in the image-level prediction? A simple solution was first proposed by Zeiler and Fergus (2014): portions of the image are successively masked out with a sliding window and the image-level responses are analyzed: if a relevant image area is masked out, image-level recognition performance should decrease. This approach has several limitations: 1) from a computational point of view, images need to be processed many times and, more importantly, 2) redundant objects will not be detected. Typically, if a medical image contains several similar lesions, masking a single lesion out may not affect the diagnosis. Other methods were proposed to quantify how much each pixel impacts the image-level prediction, while analyzing the full image: the deconvolution method (Zeiler and Fergus, 2014), the sensitivity analysis (Simonyan et al., 2014) and layer-wise relevance propagation (Bach et al., 2015). These methods allow a visualization in terms of a heatmap the size of the input image. These algorithms have in common that the image only needs to be processed twice: the image data is propagated forward through the network and gradients of the image-level predictions, or similar quantities, are propagated backwards. The simplest solution (Simonyan et al., 2014), for instance, computes the partial derivative of the image-level predictions with respect to the value of each pixel: the backpropagated quantities are partial derivatives of the image-level predictions. The most advanced solution (Bach et al., 2015) forces the backpropagated quantities to be preserved between neurons of two adjacent layers. A detailed comparison can be found in Samek et al. (2016).

3. Method Overview

Unlike other retinal image analysis methods based on deep learning, we propose to detect lesions locally in images using image-level labels only for supervision. The proposed solution improves on existing method for visualizing what ConvNets are learning. To go from visualizations designed to help understand what ConvNets are learning to visualizations useful for computer-aided diagnosis, the quality of the produced heatmaps needs to be improved. In particular, we will show that those heatmaps contain artifacts due to the architecture of ConvNets and also due to the heatmap definition itself. To address this issue, we propose to add regularization terms to the heatmaps during training. Because those heatmaps depend on backpropagated quantities, the network parameters cannot be optimized using the usual backpropagation method, so a different ConvNet training method had to be proposed: while standard training algorithms propagate image intensities through

the ConvNet and backpropagate the gradients of the optimization criterion, the proposed training algorithm involves a third pass on the ConvNet to propagate second-order gradients forward. This new training procedure can be obtained through simple adaptations of deep learning libraries. In this paper, we decided to focus on the sensitivity criterion (Simonyan et al., 2014) for its simplicity, but it could be extended to the deconvolution method (Zeiler and Fergus, 2014) or to layer-wise relevance propagation (Bach et al., 2015) as well.

4. Introduction to ConvNets

This section summarizes the main elements of a ConvNet, in order to introduce the notations used in the remaining of this paper.

4.1. Data Tensors

Let L denote the number of layers in a ConvNet. Let $D^{(l)}$, $l = 0, \dots, L$, denote the data flowing from layer l to layer $l + 1$: $D^{(0)}$ denotes the input data, $D^{(l)}$, $1 \leq l \leq L - 1$, is composed of activation maps and $D^{(L)}$ contains the image-level predictions. For faster computations, ConvNets usually process multiple images simultaneously, so $D^{(0)}$ is generally a mini-batch of N images. $D^{(l)}$ is organized as a 4th-order tensor with dimensions $N \times W_l \times H_l \times C_l$, where $W_l \times H_l$ is the size of the activation maps produced by layer l (or the size of the input images if $l = 0$) and C_l is the number of activation maps per image (or the number of color channels if $l = 0$).

4.2. Convolutional Layer (Conv)

Let $w_l \times h_l$ denote the size of the sliding window and let s_l denote its stride, i.e. the offset between two sliding window locations. The value of $D^{(l)}$ in the c^{th} activation map of the n^{th} image, at the (x, y) sliding window location, is obtained by a cross-correlation product between $D^{(l-1)}$ and a tensor $W^{(l)}$ of C_l filters with dimensions $w_l \times h_l \times C_{l-1}$ each. A bias $b_{x,y,c}^{(l)}$ is added to the product and a nonlinear activation function a_l is applied to the sum:

$$D_{n,x,y,c}^{(l)} = a_l \left(\sum_{\substack{u=-\frac{w_l}{2}, \dots, -\frac{w_l}{2}+w_l \\ v=-\frac{h_l}{2}, \dots, -\frac{h_l}{2}+h_l \\ d=1, \dots, C_{l-1}}} W_{u,v,d,c}^{(l)} D_{n,s_l x+u, s_l y+v, d}^{(l-1)} + b_{x,y,c}^{(l)} \right). \quad (1)$$

Biases are generally tied, meaning that $b_{x,y,c}^{(l)} = b_c^{(l)}$, otherwise they are said to be untied.

4.3. Activation Functions

Currently, the most popular activation functions are rectifiers and leaky rectifiers (He et al., 2015), which are much less computationally intensive than the traditional sigmoid function for instance. They can be expressed as follows:

$$r_\alpha(x) = \max(\alpha x, x), \forall x \in \mathbb{R}, \quad (2)$$

where $\alpha \in [0, 1[$ is usually small: $\alpha = 0.01$, typically, or $\alpha = 0$ in the original rectifier function. Leaky rectifiers with large α values (e.g. $\alpha = 0.33$) are called ‘very leaky rectifiers’: they allow training very deep ConvNets from scratch (He et al., 2015).

4.4. Dense or Fully-Connected Layers (Dense)

Dense layers are a special case of convolutional layers where $w_l = W_{l-1}$ and $h_l = H_{l-1}$, so the dimensions of $D^{(l)}$ are $N \times 1 \times 1 \times C_l$, where C_l is the number of neurons / filters in layer l .

4.5. Pooling Layer (MaxPool, MeanPool or RMSPool)

Pooling layers also rely on a $w_l \times h_l$ sliding window with a stride of s_l . Those layers replace the content of the sliding window in the input data tensor by a single value in the output tensor. With a stride greater than 1, a down-sampling operation is performed. Typical pooling operators are the maximum, the mean and the root mean square (RMS). Let $\mathcal{N}_l(x, y) = \{(s_l x + u, s_l y + v) \text{ s.t. } u = -\frac{w_l}{2}, \dots, -\frac{w_l}{2} + w_l, v = -\frac{h_l}{2}, \dots, -\frac{h_l}{2} + h_l\}$ denote the neighborhood of pixel location (x, y) inside $D^{(l-1)}$. A MaxPool layer computes:

$$D_{n,x,y,c}^{(l)} = \max_{(u,v) \in \mathcal{N}_l(x,y)} D_{n,u,v,c}^{(l-1)} \quad (3)$$

and a MeanPool layer computes:

$$D_{n,x,y,c}^{(l)} = \frac{1}{w_l \times h_l} \sum_{(u,v) \in \mathcal{N}_l(x,y)} D_{n,u,v,c}^{(l-1)} \quad (4)$$

Note that the number of activation maps is unchanged by those operators: $C_l = C_{l-1}$. Finally, an RMSPool layer simply derives from a MeanPool layer as follows:

$$\text{RMSPool}(D^{(l)}) = \sqrt{\text{MeanPool}(D^{(l)2})} \quad (5)$$

4.6. Network Training

The parameters of a ConvNet, namely filter weights and biases, can be optimized with the backpropagation method. This method progressively calculates the gradient of a loss function \mathcal{L}_L with respect to all the parameters, using the chain rule of derivation:

$$\frac{\partial \mathcal{L}_L}{\partial D^{(l-1)}} = \frac{\partial \mathcal{L}_L}{\partial D^{(l)}} \frac{\partial D^{(l)}}{\partial D^{(l-1)}} \quad (6)$$

$$\frac{\partial \mathcal{L}_L}{\partial \rho} = \frac{\partial \mathcal{L}_L}{\partial D^{(l)}} \frac{\partial D^{(l)}}{\partial \rho}, \rho = W^{(l)} \text{ or } b^{(l)} \quad (7)$$

Those gradients are then used by an optimizer to update the parameters, in an attempt to minimize the loss function. Loss function \mathcal{L}_L typically quantifies the classification or regression error, based on image-level predictions computed in $D^{(L)}$. To improve generalization, regularization terms are usually added to the loss function: they typically aim at minimizing the L1- or L2-norm of the filter weights.

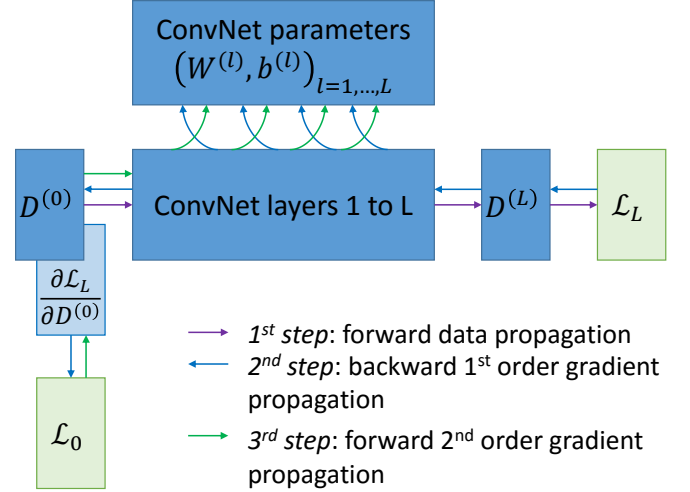


Figure 1: Backward-forward propagation method — illustration with $\lambda = 0$

4.7. Dropout and Maxout Layers

Dropout is another regularization technique (Hinton et al., 2012). During each training iteration, a random selection of filters from layer $l+1$ (one filter in p) are ‘dropped’: their input and output connections are temporarily removed. The goal is to train multiple models, where each model is a ‘thinned’ version of the ConvNet. For improved performance, a Maxout layer can be placed in position $l+2$: this operator simply returns the maximum output among subsets of p filters from layer $l+1$ (Goodfellow et al., 2013).

5. Backward-Forward Propagation Method

This section introduces a novel method for optimizing the parameters of a ConvNet when the loss function to minimize is of the form:

$$\begin{cases} \mathcal{L} &= \mathcal{L}_L + \mathcal{L}_\lambda \\ \mathcal{L}_\lambda &= g\left(\frac{\partial \mathcal{L}_L}{\partial D^{(\lambda)}}\right), 0 \leq \lambda < L \end{cases} \quad (8)$$

\mathcal{L}_λ typically is a regularity constraint on the gradients of \mathcal{L}_L . The proposed algorithm, illustrated in Fig. 1, updates each parameter tensor ρ during one training iteration, as follows:

1. The data is propagated forward through the network, from $D^{(0)}$ to $D^{(L)}$, in order to compute loss function \mathcal{L}_L .
2. The gradient of \mathcal{L}_L is propagated backward through the network, from $D^{(L)}$ to $D^{(0)}$, using equations 6 and 7. The goal is to compute $\frac{\partial \mathcal{L}_L}{\partial \rho}$, for each parameter tensor ρ , and also to compute \mathcal{L}_λ .
3. The gradient of \mathcal{L}_λ is propagated forward through the 1st order derivative of the network, from $D^{(0)}$ to $D^{(L)}$, in order to compute $\frac{\partial \mathcal{L}_\lambda}{\partial \rho}$, for each parameter tensor ρ .
4. Each parameter tensor ρ is updated proportionally to $\frac{\partial \mathcal{L}_L}{\partial \rho} + \frac{\partial \mathcal{L}_\lambda}{\partial \rho}$.

The proposed backward-forward propagation method can be implemented simply using deep learning libraries with built-in automatic differentiation, such as TensorFlow⁴. The main difficulty is to provide a forward 2nd order gradient function for each operator in the network, in order to perform step 3, while deep learning libraries only provide backward 1st order gradients. The following sections provide formulas for operators described in section 4.

5.1. Forward 2nd order Gradients for Cross-Correlation

We first discuss the main building-block of ConvNets, namely cross-correlation between data $D^{(l-1)}$ and filter weights $W^{(l)}$, used by convolutional and dense layers (cf. equation 1). Bias addition, which is trivial, is not discussed and activation is discussed in the following section. Because cross-correlation has two inputs ($D^{(l-1)}$ and $W^{(l)}$), two backward 1st order gradients need to be computed:

$$\left(\frac{\partial \mathcal{L}_L}{\partial D^{(l-1)}}\right)_{n,x,y,d} = \sum_{\substack{u=-\frac{w_l}{2}, \dots, -\frac{w_l}{2}+w_l \\ v=-\frac{h_l}{2}, \dots, -\frac{h_l}{2}+h_l \\ c=1, \dots, C_l}} W_{x,y,d,c}^{(l)} \left(\frac{\partial \mathcal{L}_L}{\partial D^{(l)}}\right)_{n,s_l x-u, s_l y-v, c}, \quad (9)$$

$$\left(\frac{\partial \mathcal{L}_L}{\partial W^{(l)}}\right)_{x,y,d,c} = \sum_{\substack{u=-\frac{w_l}{2}, \dots, -\frac{w_l}{2}+w_l \\ v=-\frac{h_l}{2}, \dots, -\frac{h_l}{2}+h_l \\ n=1 \dots N}} \left(\frac{\partial \mathcal{L}_L}{\partial D^{(l)}}\right)_{n,x,y,c} D_{n,s_l x+u, s_l y+v, d}^{(l-1)}. \quad (10)$$

These equations derive from the chain rule of derivation (equation 7) and the differentiation of a cross-correlation product (Nielsen, 2015). We can see that the cross-correlation between $W^{(l)}$ and $D^{(l-1)}$ in the forward transform (equation 1) becomes an actual convolution product between $W^{(l)}$ and $\frac{\partial \mathcal{L}_L}{\partial D^{(l)}}$ in the backward 1st order gradient (equation 9). As expected, one can verify that it becomes a cross-correlation product again, between $W^{(l)}$ and $\frac{\partial \mathcal{L}_L}{\partial D^{(l-1)}}$, in the forward 2nd order gradient:

$$\left(\frac{\partial \mathcal{L}_L}{\partial D^{(l)}}\right)_{n,x,y,c} = \sum_{\substack{u=-\frac{w_l}{2}, \dots, -\frac{w_l}{2}+w_l \\ v=-\frac{h_l}{2}, \dots, -\frac{h_l}{2}+h_l \\ d=1, \dots, C_{l-1}}} W_{u,v,d,c}^{(l)} \left(\frac{\partial \mathcal{L}_L}{\partial D^{(l-1)}}\right)_{n,s_l x+u, s_l y+v, d}. \quad (11)$$

The gradient of the loss function with respect to $W^{(l)}$ is a cross-correlation product between $\frac{\partial \mathcal{L}_L}{\partial D^{(l)}}$, playing the role of a filter, and the input data (equation 10). One can verify that the same applies during the forward pass, where $\frac{\partial \mathcal{L}_L}{\partial D^{(l-1)}}$ plays the role of the input data:

$$\left(\frac{\partial \mathcal{L}_L}{\partial W^{(l)}}\right)_{x,y,d,c} = \sum_{\substack{u=-\frac{w_l}{2}, \dots, -\frac{w_l}{2}+w_l \\ v=-\frac{h_l}{2}, \dots, -\frac{h_l}{2}+h_l \\ n=1 \dots N}} \left(\frac{\partial \mathcal{L}_L}{\partial D^{(l)}}\right)_{n,x,y,c} \left(\frac{\partial \mathcal{L}_L}{\partial D^{(l-1)}}\right)_{n,s_l x+u, s_l y+v, d}. \quad (12)$$

⁴<https://www.tensorflow.org> — one line implementation of the \mathcal{L}_L cost function, if g is the L1-norm: `tf.add_to_collection('losses', tf.reduce_sum(tf.abs(tf.gradients(L_L, [D_1])[0])))`

5.2. Forward 2nd order Gradient for the Leaky Rectifier

Let $y = r_\alpha(x) = \max(\alpha x, x)$ with $\alpha \in [0, 1[$ (cf. equation 2). Because r_α simply is a piecewise linear operator, the backward 1st order gradient for r_α is given by:

$$\frac{\partial \mathcal{L}_L}{\partial x} = \begin{cases} 0 & \text{if } \alpha = 0 \text{ and } x < 0 \\ \frac{1}{\alpha} \frac{\partial \mathcal{L}_L}{\partial y} & \text{if } \alpha > 0 \text{ and } x < 0 \\ \frac{\partial \mathcal{L}_L}{\partial y} & \text{if } x \geq 0 \end{cases} \quad (13)$$

and the forward 2nd order gradient is given by:

$$\frac{\partial \mathcal{L}_L}{\partial y} = \begin{cases} \alpha \frac{\partial \mathcal{L}_L}{\partial x} & \text{if } x < 0 \\ \frac{\partial \mathcal{L}_L}{\partial x} & \text{if } x \geq 0 \end{cases}. \quad (14)$$

Note that the test for choosing the multiplicative factor (1 or α) is always triggered by the operator's input (x). The same applies to the MaxPool operator below.

5.3. Forward 2nd order Gradient for MaxPool

The backward 1st order gradient for MaxPool (cf. equation 3) is given by:

$$\left(\frac{\partial \mathcal{L}_L}{\partial D^{(l-1)}}\right)_{n,x,y,c} = \sum_{\substack{u,v \\ \text{s.t. } D_{n,u,v,c}^{(l)} = D_{n,x,y,c}^{(l-1)}}} \left(\frac{\partial \mathcal{L}_L}{\partial D^{(l)}}\right)_{n,u,v,d}. \quad (15)$$

This means that the errors are backpropagated to the winning neuron inside each sliding window location. One can verify that the forward 2nd order gradient is given by:

$$\left(\frac{\partial \mathcal{L}_L}{\partial D^{(l)}}\right)_{n,x,y,c} = \left(\frac{\partial \mathcal{L}_L}{\partial D^{(l-1)}}\right)_{\text{argmax}(D_{n,x,y,c}^{(l)})}, \quad (16)$$

where $\text{argmax}(D_{n,x,y,c}^{(l)})$ returns the index of the winning neuron inside the corresponding sliding window in $D^{(l-1)}$.

5.4. Forward 2nd order Gradient for MeanPool

The backward 1st order gradient for MeanPool (cf. equation 4) is given by:

$$\left(\frac{\partial \mathcal{L}_L}{\partial D^{(l-1)}}\right)_{n,x,y,c} = \frac{1}{w_l \times h_l} \sum_{\substack{u,v \\ \text{s.t. } (x,y) \in \mathcal{N}_l(u,v)}} \left(\frac{\partial \mathcal{L}_L}{\partial D^{(l)}}\right)_{n,u,v,c}. \quad (17)$$

This means that, during backpropagation, the errors are equally distributed to all neurons inside each sliding window location. The forward 2nd order gradient is a special case of equation 11, where W_l is a mean filter; it is given by:

$$\left(\frac{\partial \mathcal{L}_L}{\partial D^{(l)}}\right)_{n,x,y,c} = \frac{1}{w_l \times h_l} \sum_{(u,v) \in \mathcal{N}_l(x,y)} \left(\frac{\partial \mathcal{L}_L}{\partial D^{(l-1)}}\right)_{n,u,v,c}. \quad (18)$$

In other words, the forward 2nd order gradient for MeanPool is MeanPool itself.

5.5. Forward 2nd order for Dropout and Maxout

Dropout does not need to be addressed specifically as it simply alters the network temporarily: the above 1st order and 2nd order gradients are simply computed in the thinned network. As for Maxout, it is addressed similarly to the other maximum-based operators (leaky rectifiers and MaxPool).

6. Heatmap Generation and Optimization

The general-purpose optimization method above is now applied to a problem of particular interest in medical image analysis tasks, namely lesion detection. Sensitivity analysis is used to visualize the local features used by ConvNets in their attempt to produce predictions at the image level. We show how training ConvNets with the backward-forward optimization method can improve that visualization, i.e. can improve detection performance at the pixel level.

6.1. Notations

We remind that $D^{(0)}$, the ConvNet’s input, is a mini-batch of N images with dimensions $W_0 \times H_0$ and depth C_0 , where $C_0 = 3$ for color images. Let $f : \mathbb{R}^{N \times W_0 \times H_0 \times C_0} \rightarrow \mathbb{R}$ denote a function of interest computed by the ConvNet. This function may be the loss function \mathcal{L}_L or the prediction for one image if $N = 1$.

6.2. Sensitivity Criterion

In sensitivity analysis, the contribution of $D_{n,x,y,c}^{(0)}$ to $f(D^{(0)})$ is assessed by the absolute value of the partial derivative of $f(D^{(0)})$ with respect to $D_{n,x,y,c}^{(0)}$, which can be computed according to equation 6. The overall contribution $\omega_{n,x,y}$ of pixel $D_{n,x,y}^{(0)}$ can be summarized as follows (Simonyan et al., 2014):

$$\omega_{n,x,y} = \left\| \left(\frac{\partial f(D^{(0)})}{\partial D_{n,x,y,c}^{(0)}} \right)_{c \in \{r,g,b\}} \right\|_q, \quad (19)$$

where $\|\cdot\|_q, q \in \mathbb{N}$, denotes the q -norm; Simonyan et al. (2014) used $q = \infty$.

6.3. Interpretation

The sensitivity criterion indicates which local changes would modify the target function. In the context of DR screening, this can be interpreted as follows. Let us assume that a fundus image is referable and classified as such by the ConvNet. In that case, any lesion should be associated with nonzero ω values, as removing the lesion might downgrade the diagnosis and enhancing the lesion would consolidate it. Now, let us assume that the image is nonreferable and classified as such by the ConvNet. In that case, subtle microaneurysms in mild nonproliferative DR patients, which are not referable yet, should be associated with nonzero ω values. Indeed, more pronounced microaneurysms would possibly upgrade the diagnosis to referable DR. So, in both cases, lesions should be detected by the ω criterion.

Although this criterion has interesting features for lesion detection, it also has a few drawbacks: two types of artifacts may appear, so we had to modify this criterion accordingly.

6.4. Hue-Constrained Sensitivity Criterion

The first limitation of this criterion is that lesion confounders may also be associated with nonzero ω values: dust on the camera’s lens resembling microaneurysms, specular reflections resembling exudates or cotton-wool spots, etc. Indeed, modifying a confounder could make it resemble a true lesion even more. Typically, by changing one or two color channels only, the confounder would have a more compatible color. This behavior will produce false alarms, that we will refer to as a ‘disguise artifacts’.

The solution we propose to reduce those artifacts is to constrain the allowed local changes. Specifically, we force these changes to preserve the hue, so that sensitivity analysis essentially focuses on pattern enhancements or attenuations. Hue preservation is ensured by forcing all three color components of a pixel to be multiplied by the same factor. So, instead of computing the sensitivity of each color component independently and combining them afterwards (following equation 19), a single sensitivity value $\pi_{n,x,y}$ is computed per pixel in a single operation, as described hereafter. Given the input tensor $D^{(0)}$ with dimensions $N \times W_0 \times H_0 \times C_0$, a binary tensor m with dimensions $N \times W_0 \times H_0 \times 1$ is defined. The proposed hue-constrained sensitivity criterion is given by:

$$\pi_{n,x,y} = \left| \frac{\partial f(m * D^{(0)})}{\partial m_{n,x,y}} \right|, \quad (20)$$

where tensor m is filled with ones and where ‘*’ denotes the element-wise tensor multiplication, which implies that $m * D^{(0)} = D^{(0)}$. Following the usual convention, the fact that the fourth dimension of m is 1 implies that all color components of a pixel in $D^{(0)}$ are multiplied by the same tensor element in m , which ensures the desired hue preservation property.

6.5. Sparsity-Enhanced Sensitivity Criterion

The second and most important limitation of the sensitivity criterion is that confounders in the vicinity of true lesions tend to be amplified. This effect, illustrated in Fig. 2, is due to down-sampling, which occurs in pooling or convolutional layers with a stride greater than 1. Indeed, according to the chain rule of derivation (equation 6), the gradient of $f(D^{(0)})$ with respect to $D^{(0)}$ is obtained by multiplying the following partial derivative tensors: $\frac{\partial D^{(1)}}{\partial D^{(0)}}, \dots, \frac{\partial D^{(L)}}{\partial D^{(L-1)}}, \frac{\partial \mathcal{L}_L}{\partial D^{(L)}}$. Because of down-sampling, these partial derivative tensors are of decreasing sizes. As a result, a true lesion and confounders in its vicinity share common terms in the expression of their influence on $f(D^{(0)})$. These terms tend to be large because of the true lesion, so the perceived influence of the confounders are artificially boosted. We will refer to those amplified false alarms as ‘drafting artifacts’.

A brute-force solution for reducing those artifacts would be to 1) compute the π tensor according to equation 20, 2) record the maximal π_{n,x^*,y^*} values and 3) set the corresponding m_{n,x^*,y^*} values to zero. Then, the π tensor should be computed again using the modified m tensor, in order to record the next largest $\pi_{n,x^{**},y^{**}}$ values, without the drafting influence of the (n, x^*, y^*) pixels. And so on until the influence of each pixel has been

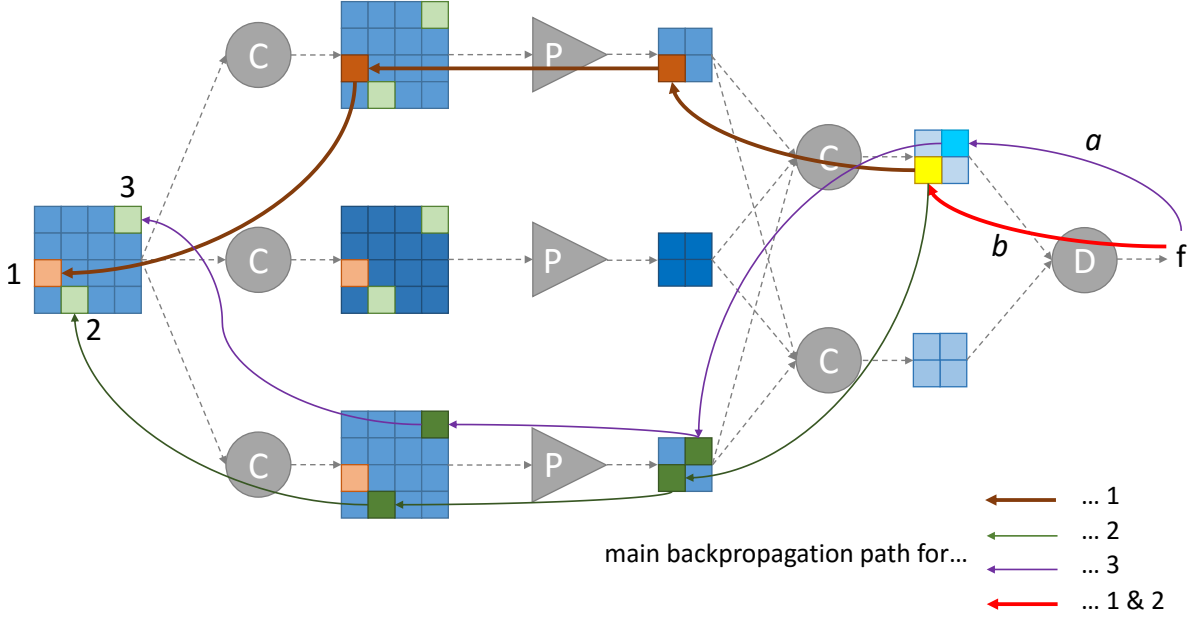


Figure 2: Illustrating drafting artifacts: one lesion ('1', in red) and two confounders ('2' and '3', in green) are processed by a simplistic ConvNet. Convolution operations (stride = 1) and max-pooling operations (size = 2 X 2, stride = 2) are indicated by letters 'C' and 'P', respectively; dense layers are indicated by letter 'D'. Colors in intermediate feature maps represent the contribution of each input pattern (red + green → yellow, green + blue → cyan). Because pattern '1' is a lesion, partial derivatives associated with edges along its backpropagation paths (such as edge 'b') tend to be larger (compared to edge 'a' in particular). Because they are neighbors, patterns '1' and '2' share the first edge ('b') along their main backpropagation path. So, even though patterns '2' and '3' are identical, the sensitivity of output 'f' with respect to '3', obtained by multiplying partial derivatives along its backpropagation paths, is smaller than the sensitivity with respect to '2', which benefits from a drafting effect from '1'.

recorded independently from its more influential neighbors. However, the complexity of this solution clearly is prohibitive.

Instead, we propose an indirect solution which reduces drafting artifacts while training the ConvNet, so that we do not have to deal with them explicitly afterwards. In that purpose, an additional term \mathcal{L}_λ , $\lambda = 0$, is added to the total loss function \mathcal{L} . The aim of \mathcal{L}_0 is to maximize the sparsity of ω or π . By forcing the ConvNet to reduce the number of nonzero pixels in ω or π , while maintaining its classification or regression accuracy, the ConvNet has to modify its parameters in such a way that true lesions and confounders in their vicinity share as little large terms as possible in the expression of their influence on $f(D^{(0)})$. In other words, the ConvNet is forced to build more discriminative filters: filters that better separate true lesions from confounders. Following Tibshirani (1996), the sparsity of ω or π is maximized through L1-norm minimization, rather than L0-norm minimization, which is NP-hard.

The sparsity of ω can be enhanced using the proposed backward-forward method. In this case, $f(D^{(0)})$ in equation 19 is \mathcal{L}_L and function g in equation 8 is the L1-norm, multiplied by a factor ν . The sparsity of π can be enhanced similarly: in this case, the role of the input data tensor is played by tensor m (see equation 20).

7. Experiments

The proposed heatmap generation and optimization solution is now evaluated in the context of diabetic retinopathy screening, using a ConvNet specifically designed for this task.

7.1. Baseline ConvNet

This section introduces the ConvNet that we used in our experiments. This ConvNet produces predictions at the image level; based on modifications described in section 6, it also produces predictions at the pixel level. Successful solutions based on ConvNets were submitted to the 2015 Diabetic Retinopathy competition and the source code of the best three solutions is publicly available. Rather than reinventing the wheel, we used the best of these solutions to set up our baseline ConvNet.

7.1.1. Image Preprocessing and Data Augmentation

Image preprocessing was adapted from the min-pooling solution,⁵ by B. Graham, which ranked first in the Kaggle Diabetic Retinopathy competition. Let I denote the input image. The width of the camera's field of view in I is estimated and I is resized to normalize that width to 512 pixels. The background I_b of the resulting I_r image is then estimated by a large

⁵<https://www.kaggle.com/c/diabetic-retinopathy-detection/forums/t/15801/competition-report-min-pooling-and-thank-you>

Gaussian filter in each color channel (standard deviation: 8.5 pixels). A normalized image is defined as $I_n = 4(I_r - I_b)$. Finally, because the camera’s field of view usually contains illumination artifacts around its edges, the field of view is eroded by 5% in I_n . Following all the top ranking solutions in the competition, data augmentation is performed during training. Before feeding a preprocessed image to the network, the image is randomly rotated (range: $[0^\circ, 360^\circ]$), translated (range: $[-10 \text{ px}, 10 \text{ px}]$), scaled (range: $[85\%, 115\%]$), horizontally flipped and its contrast is modified (multiplicative factor range: $[60\%, 167\%]$); different transformation parameters are generated at each epoch. The resulting image is resized and cropped to 448 x 448 pixels.

7.1.2. Network Structure

The network structure used in this study was adapted from the o_O solution,⁶ by M. Antony and S. Brüggemann, which ranked second in the Kaggle Diabetic Retinopathy competition. This solution was selected since it relies on networks composed exclusively of basic processing units implemented in all deep learning libraries. This property does not apply to the min-pooling solution, in particular, which relies on specialized operations such as fractional max pooling (Graham, 2014).

The o_O solution relies on two networks, namely ‘net A’ and ‘net B’, applied to images of size 448 x 448 pixels. It also relies on two sub-networks of ‘net A’ and ‘net B’ applied to smaller images (224 x 224 pixels and 112 x 112 pixels). The designers of o_O noticed that ‘net B’ alone works almost as well as the ensemble, so we focused on ‘net B’ in this study. Its structure is described in table 1. All convolutional and dense layers use untied biases and leaky rectifiers as activation functions. The last dense layer with a single unit is used for regression, to predict the image label.

7.1.3. Network Training

Following o_O, networks are trained to minimize the mean squared error between image labels and predictions. Additionally, L2 regularization with factor 0.0005 is applied to filter weights in all convolutional and dense layers.

In the original o_O solution, (sub-)networks are trained sequentially by increasing size: larger networks are initialized with the optimal weights found for the smaller networks. This ad-hoc procedure is not convenient: visual inspections may be needed to decide when a network is trained enough and that the next network should be trained. It adds subjectivity to the training process and makes it less automatic. However, as noted by the designers, ‘net A’ and ‘net B’ can be trained directly if very leaky rectifiers ($\alpha = 0.33$) are used instead of leaky rectifiers ($\alpha = 0.01$). Although that solution turned out to be less efficient in o_O, we were able to fill the gap using an Adam optimizer (Kingma and Ba, 2015), instead of the Nesterov momentum optimizer (Nesterov, 1983) used in o_O. A learning rate of 0.0001 was used initially. Following common practice,

we manually decreased the learning rate by a factor of 10 when performance in the validation step stopped increasing.

7.2. Implementation Details

The proposed algorithms were implemented in C++ and Python using OpenCV⁷ for image preprocessing and data augmentation, and TensorFlow for network training and inference. Forward 2nd order derivatives were implemented in Python when possible; that of MaxPool was implemented in C++. One GPU card was used: a GeForce GTX 1070 by Nvidia. Training and testing were performed using mini-batches of $N = 36$ images, in accordance with the memory capacity of the GPU card (7.92 GiB).

7.3. Datasets

Two datasets were used in this study: the ‘Kaggle Diabetic Retinopathy’ dataset, used for training and testing at the image level, and ‘DiaretDB1’, used for testing at the lesion level.

7.3.1. Kaggle Diabetic Retinopathy Dataset

The first dataset consists of 88,702 color fundus photographs from 44,351 patients: one photograph per eye.⁸ Images were captured with various digital fundus cameras, in multiple primary care sites throughout California and elsewhere. Their definitions range from 433 x 289 pixels to 5184 x 3456 pixels (median definition: 3888 x 2592 pixels). Those images were then uploaded to EyePACS, a free platform for DR screening (Cuadros and Bresnick, 2009). For each eye, DR severity was graded by a human reader according to the ETDRS scale (Wilkinson et al., 2003): ‘absence of DR’, ‘mild non-proliferative DR (NPDR)’, ‘moderate NPDR’, ‘severe NPDR’ and ‘proliferative DR (PDR)’. The dataset was split into a training set (35,126 images from 17,563 patients) and a test set (53,576 images from 26,788 patients): those two sets are referred to as ‘Kaggle-train’ and ‘Kaggle-test’, respectively. Networks were trained on 80 % of the Kaggle-train dataset (the first 28,100 images) and validated on the remaining 20 % (the last 7,024 images).

For the purpose of this study, about DR screening, severity grades were grouped into two categories: nonreferable DR (absence of DR or mild NPDR) versus referable DR (moderate NPDR or more). The prevalence of referable DR was 19.6 % in Kaggle-train and 19.2 % in Kaggle-test.

7.3.2. DiaretDB1 Dataset

The second dataset consists of 89 color fundus photographs collected at the Kuopio University Hospital, in Finland (Kauppi et al., 2007). Images were captured with the same fundus camera, a ZEISS FF450*plus* digital camera with a 50 degree field-of-view. Images all have a definition of 1500 x 1152 pixels. Independent markings were obtained for each image from four

⁶<https://www.kaggle.com/c/diabetic-retinopathy-detection/forums/t/15617/team-o-o-solution-summary>

⁷<http://opencv.willowgarage.com/>

⁸<https://www.kaggle.com/c/diabetic-retinopathy-detection/data>

id	layer type	activation maps	window size	window stride	output tensor size
1	Input				448 x 448
2	Conv	32	4 x 4	2	224 x 224
3	Conv	32	4 x 4	1	225 x 225
4	MaxPool	\emptyset	3 x 3	2	112 x 112
5	Conv	64	4 x 4	2	56 x 56
6	Conv	64	4 x 4	1	57 x 57
7	Conv	64	4 x 4	1	56 x 56
8	MaxPool	\emptyset	3 x 3	2	27 x 27
9	Conv	128	4 x 4	1	28 x 28
10	Conv	128	4 x 4	1	27 x 27
11	Conv	128	4 x 4	1	28 x 28
12	MaxPool	\emptyset	3 x 3	2	13 x 13
13	Conv	256	4 x 4	1	14 x 14
14	Conv	256	4 x 4	1	13 x 13
15	Conv	256	4 x 4	1	14 x 14
16	MaxPool	\emptyset	3 x 3	2	6 x 6
17	Conv	512	4 x 4	1	5 x 5
18	RMSPool	\emptyset	3 x 3	2	2 x 2
19	Dropout	\emptyset			
20	Dense	1024			
21	Maxout	512			
22	Dropout	\emptyset			
23	Dense	1024			
24	Maxout	512			
25	Dense	1			

Table 1: Network Structure — ‘net B’ from the o_O solution.

medical experts. The experts were asked to manually delineate the areas containing microaneurysms (or ‘small red dots’), hemorrhages, hard exudates and cotton wool spots (or ‘soft exudates’) and to report their confidence ($< 50\%$, $\geq 50\%$, 100%) for each segmented object. Based on these annotations, only five images in the dataset are considered normal: none of the experts suspect these images to contain any lesions.

Given a target lesion type, Kauppi et al. (2007) proposed a standardized procedure to evaluate the performance of a lesion detector in the DiaretDB1 dataset. In this purpose, one probability map was constructed per image: this map was obtained by averaging, at the pixel level, confidences from all four experts for the target lesion type. If and only if this map contains at least one pixel with an average confidence level above 75% , then the image is considered to contain the target lesion. Based on this criterion, a receiver-operating characteristic (ROC) curve can be constructed for the lesion detector.

7.4. Performance of the ConvNet during Training

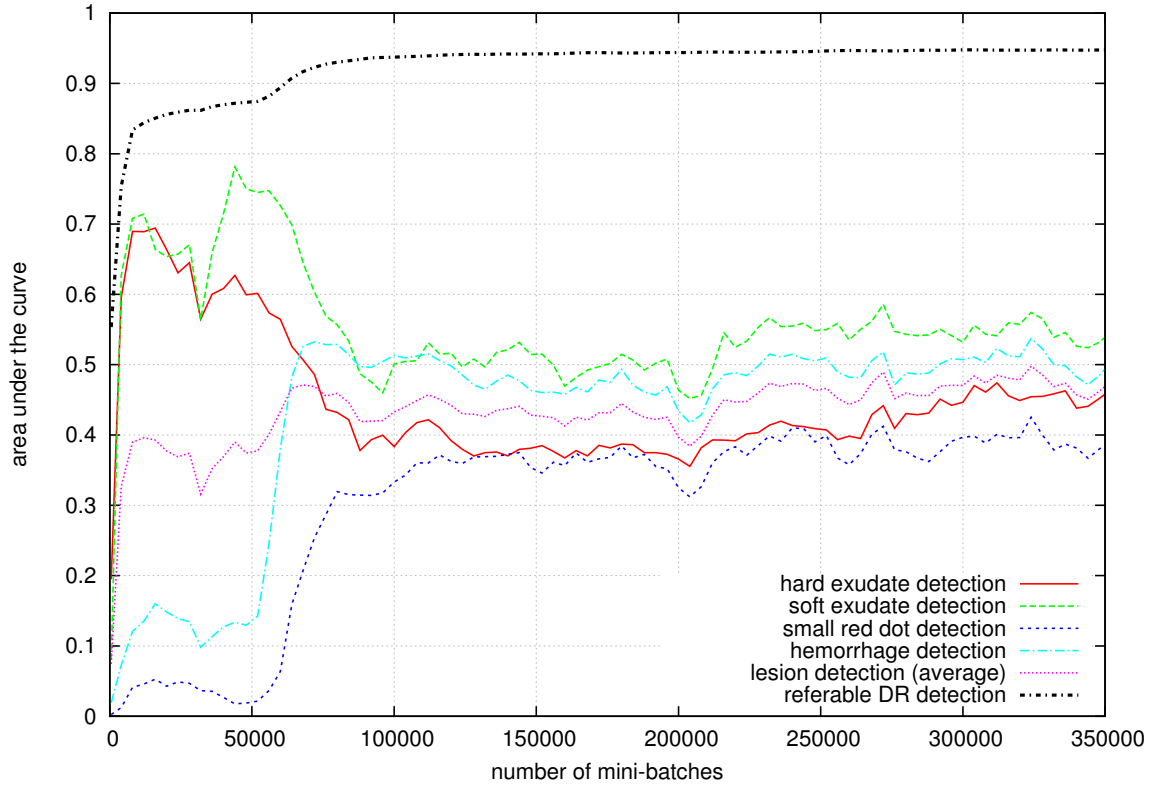
Figure 3 reports performance in the validation sets during training, using the hue-constrained sensitivity criterion, with or without sparsity maximization. Performance at the image level was assessed using a ROC analysis in the validation subset of Kaggle-train: the area A_z under the ROC curve is used as performance metric. Performance at the pixel level was assessed using a free-response ROC (FROC) analysis in the DiaretDB1

ν	image level A_z	pixel level \bar{A}_z
0	0.948	0.499
10^{-4}	0.948	0.543
10^{-3}	0.947	0.600
10^{-2}	0.546	0.375

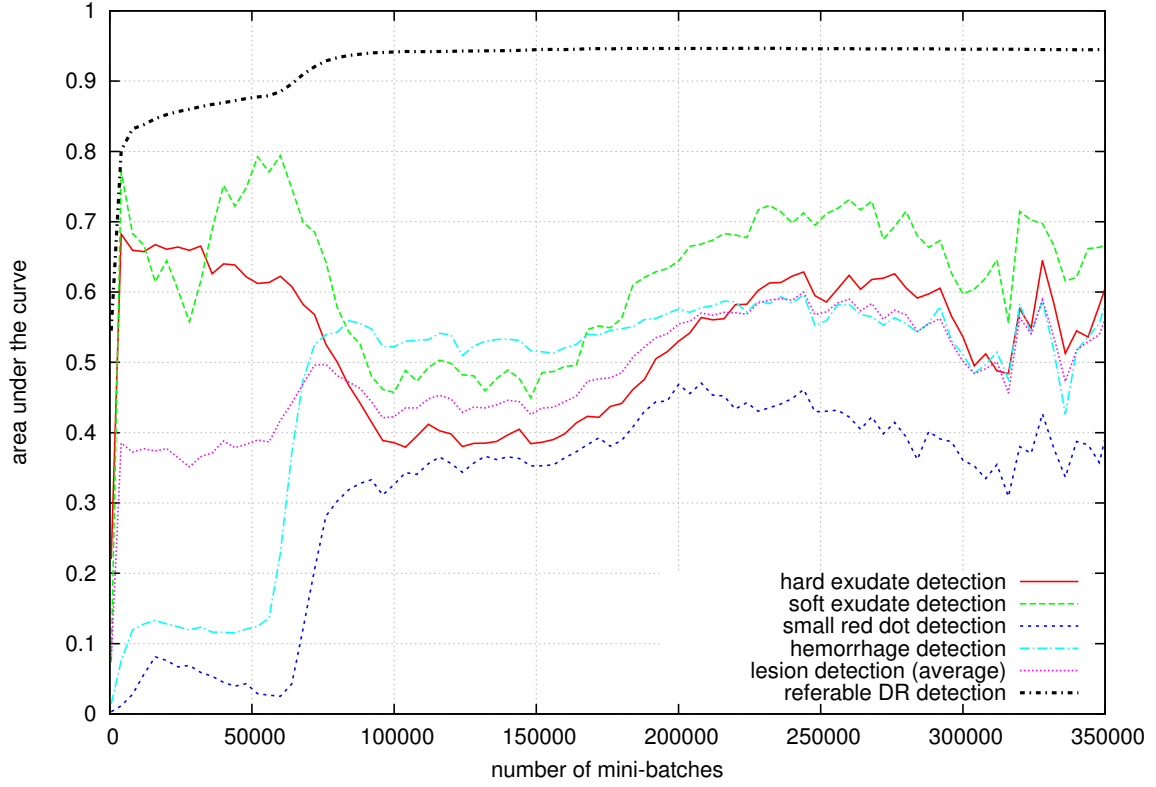
Table 2: Influence of ν , the factor of the \mathcal{L}_0 cost function, on performance — the retained solution is in bold.

dataset. FROC curves are usually not bounded along the x-axis (the number false positives per image): we used as performance metric the area A_z under the FROC curve for $0 \leq x \leq \mu$, divided by μ (with $\mu = 10$). Performance is computed for each lesion type independently, and an average performance metric \bar{A}_z is also computed. The influence of ν , the factor of the \mathcal{L}_0 cost function, on the performance at the image level (A_z in the Kaggle validation set) and at the pixel level (\bar{A}_z in the DiaretDB1 dataset), is given in table 2.

The best FROC for each lesion type is reported in Fig. 4. Figure 4 shows that the number of false alarms is rather large, particularly in the case of microaneurysm detection. The reason is that human experts primarily segmented the most obvious lesions, while screening algorithms need to focus on the most subtle lesions as well. In other words, many true lesions are



(a) Hue-constrained sensitivity criterion — factor of the \mathcal{L}_0 cost function: $\nu = 0$



(b) Hue-constrained and sparsity-enhanced sensitivity criterion — factor of the \mathcal{L}_0 cost function: $\nu = 10^{-3}$

Figure 3: Performance in the validation sets — ROC analysis in Kaggle (validation) and FROC analysis in DiaretDB1

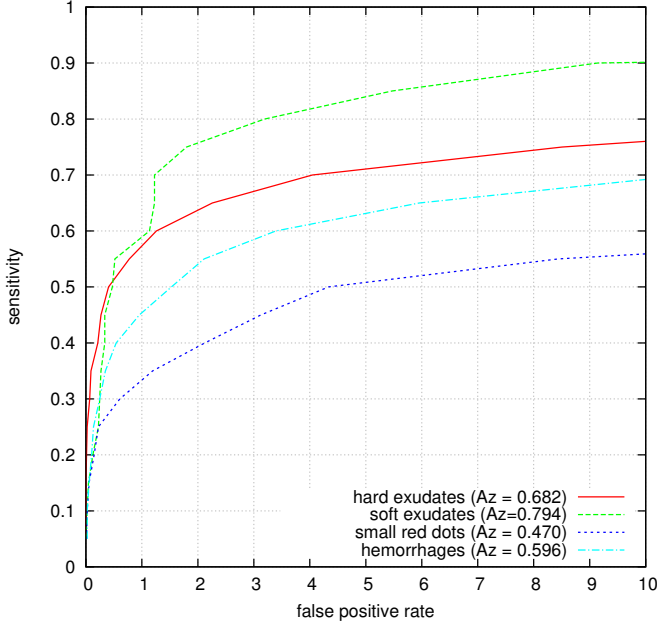


Figure 4: Lesion detection performance in DiaretDB1, at the object level

counted as false alarms. Of course, this comment also applies to competing automatic solutions. To show the value of our detections, the proposed solution was compared in Fig. 5 to results reported in the literature, following the DiaretDB1 standardized procedure (see section 7.3.2). Most authors reported a single (sensitivity, specificity) pair: this is what we reported in Fig. 5. Some authors reported ROC curves; in that case, we also reported a single (sensitivity, specificity) pair: the one closest to the (sensitivity = 1, specificity = 1) coordinate. Note that all competing solutions (Kauppi et al., 2007; Yang et al., 2013; Franklin and Rajan, 2014; Kumar et al., 2014; Bharali et al., 2015; Mane et al., 2015; Dai et al., 2016) are trained at the lesion level, while ours is trained (in Kaggle-train) at the image level.

7.5. Ensemble Learning

As commonly done in machine learning competitions (Rusakovsky et al., 2015), an ensemble of ConvNets was used to boost performance. As less commonly done, all ConvNets in the ensemble originate from the same network, but with parameter values obtained at different checkpoints during the learning process. This way, training the ensemble is not significantly more computationally intensive than training a single ConvNet. As shown in Fig. 3, individual lesion types are not optimally detected after the same number of iterations. So, the idea was to export parameter values from the ConvNet when:

1. hard exudates were optimally detected (network \mathcal{N}_{HE} — iteration 4,000),
2. soft exudates were optimally detected (network \mathcal{N}_{SE} — iteration 60,000),

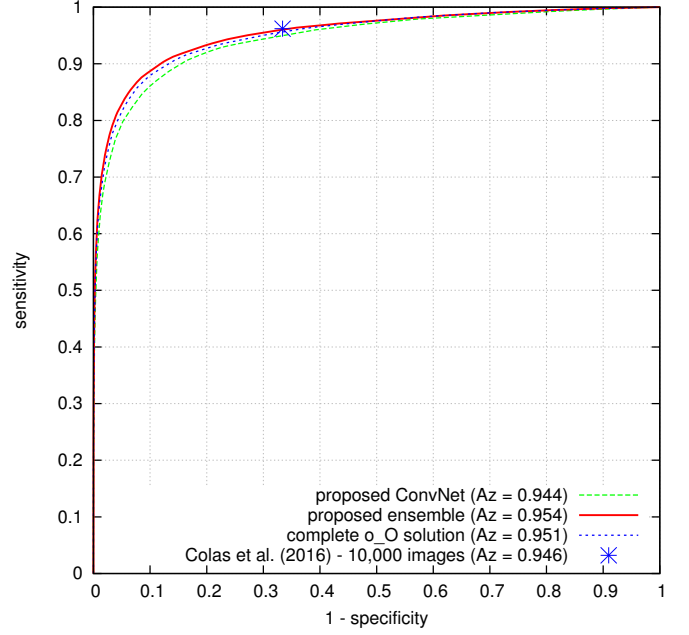
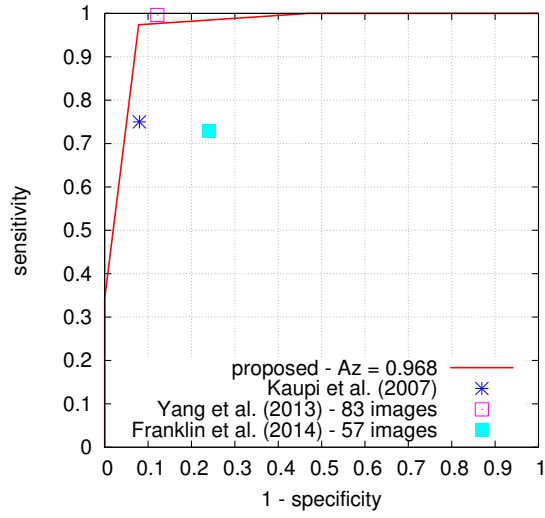


Figure 6: Referable diabetic retinopathy detection in Kaggle-test.

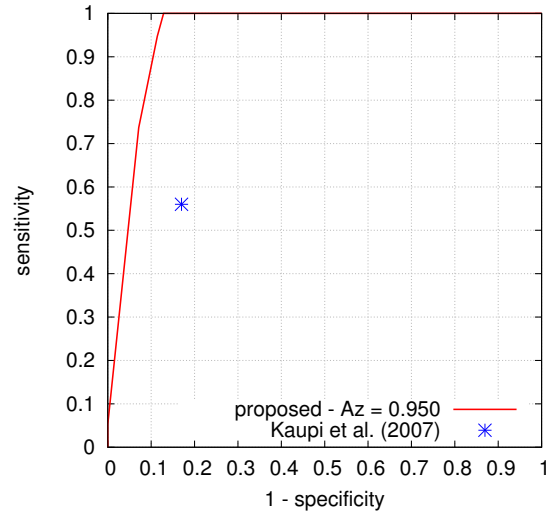
3. small red dots were optimally detected (network \mathcal{N}_{SRD} — iteration 208,000),
4. hemorrhages were optimally detected (network \mathcal{N}_H — iteration 244,000),
5. lesions were optimally detected on average (network \mathcal{N}_{AVG} — iteration 328,000),
6. referable DR was optimally detected (network \mathcal{N}_{RDR} — iteration 224,000).

Network predictions were computed for the current eye, but also for the contralateral eye, so 12 features were fed to the ensemble classifier per eye. Following the min-pooling solution, a random forest was used to build the ensemble. The full Kaggle-train dataset was used for training the random forest. Random forest parameters, the number of trees n_T and the maximum depth of each tree d_T , was optimized by 5-fold cross-validation in Kaggle-train: $n_T = 500$, $d_T = 25$. Performance in Kaggle-test is reported in Fig. 6. It is important to notice that using such an ensemble of ConvNets does not necessarily turn the solution into a black box. Indeed, the heatmaps associated with the above ConvNets all have the same size. So, to support decision for a given patient, the heatmaps associated with all the networks involved in the decision process can be blended (one blended heatmap per eye). Furthermore, each heatmap can be weighted by the importance of the associated ConvNet in the decision process.

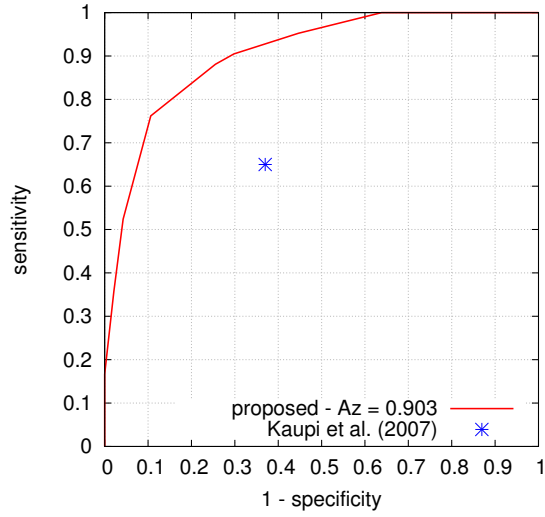
The performance of the proposed pixel-level detector is illustrated in Fig. 7 and 8 on two images from independent datasets. The first image comes from the publicly-available Messidor



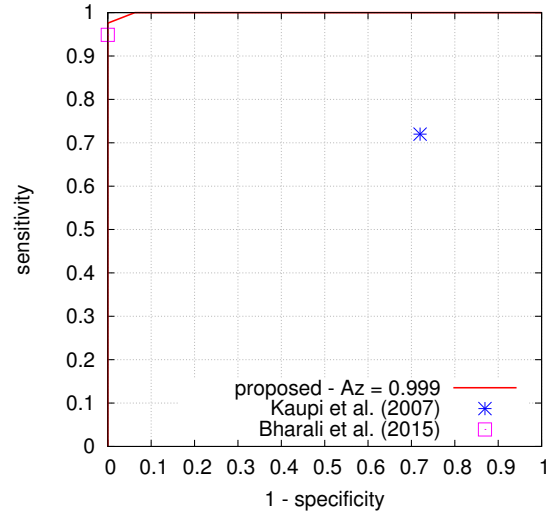
(a) Hard exudates



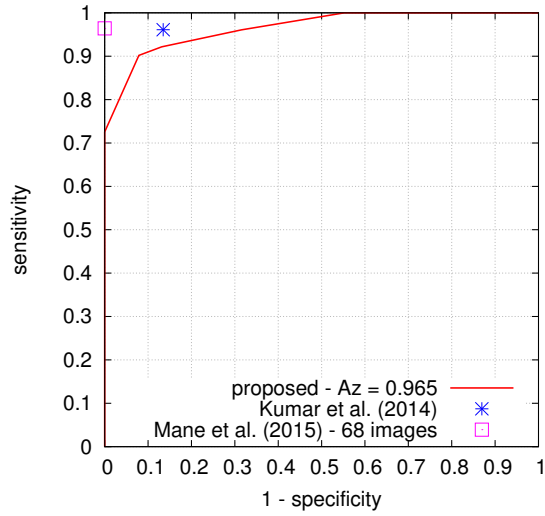
(b) Soft exudates



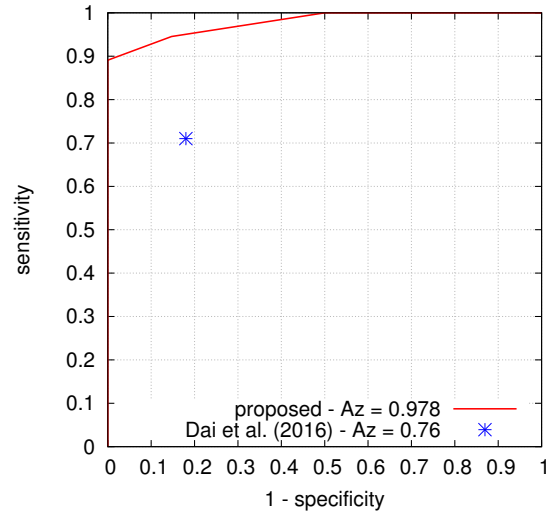
(c) Small red dots



(d) Hemorrhages



(e) Red lesions (hemorrhages and small red dots)



(f) All lesions

Figure 5: Lesion detection performance in DiaretDB1, at the image level

dataset⁹. The second image comes from a private dataset acquired with a low-cost handheld retinograph (Queliec et al., 2016a).

8. Discussion and Conclusions

A solution was proposed in this paper for the automatic detection of referable diabetic retinopathy (DR) and for the automatic detection of lesions related to DR. Unlike competing solutions, this lesion detector is trained using image-level labels only for supervision. The solution relies on a ConvNet trained to detect referable DR at the image level. Using a modified sensitivity analysis, the pixels playing a role in the image-level predictions are detected: a heatmap the size of the image is obtained. In order to improve the quality of the heatmaps (attenuate artifacts), we proposed to enhance the sparsity of the heatmaps while training the ConvNet. Because those heatmaps depend on backpropagated quantities, the network parameters cannot be optimized using the usual backpropagation method, so a different ConvNet training method was proposed.

The ConvNet, trained at the image level in the Kaggle-train dataset, was evaluated at the pixel level in the DiaretDB1 dataset (see Fig. 5). For all lesions or groups of lesions, with the exception of ‘red lesions’, the proposed framework outperforms previous solutions, even though these solutions were trained at the pixel level. This validates the relevance of image-level supervision for lesion detectors. As illustrated in two examples (see Fig. 7 and 8), the produced heatmaps are of very good quality. In particular, the false alarms detected on the vessels, in the vicinity of true lesions in the unoptimized heatmaps (π_0 maps), are strongly reduced with sparsity maximization (π_{HE} , π_{RDR} , $\bar{\pi}$). Note that detection performance is not affected much by image quality: very good detections are produced in the blurry image obtained with a low-cost, handheld retinograph (see Fig. 8). This is a very important feature, which opens the way to automated mobile screening.

Besides analyzing the pixel-level performance of the final ConvNet, we also analyzed the pixel-level performance while the ConvNet is being trained (see Fig. 3). It turned out to be quite instructive. By analyzing performance at the image level alone (the area under the ROC curve in the Kaggle validation set), all we can see is that 1) performance quickly reaches a satisfactorily level ($A_z \simeq 0.85$), then 2) slowly increases for many iterations, 3) experiences a second leap to reach a very high level ($A_z \simeq 0.93$) and finally 4) reaches its optimal state ($A_z \simeq 0.95$) very slowly. By analyzing the heatmaps, we understand that the ConvNet very quickly learns to detect exudates and cotton-wool spots (or ‘soft exudates’). The second performance leap is observed when the ConvNet learns to detect hemorrhages. The final fine-tuning stage correlates with the progressive discovery of microaneurysms (or ‘small red dots’) by the ConvNet. The order in which lesions are discovered by the ConvNet makes sense: the most obvious lesions (the largest

and the most contrasted) are detected first and then the ConvNets understands that more subtle lesions (which are more difficult to capture) are in fact more useful to make a diagnosis. By the way, we observe that the detection performance of bright lesions (exudates and cotton-wool spots) decreases when red lesions (hemorrhages and microaneurysms) are discovered: red lesions are indeed usually enough for detecting referable DR. The main difference between the two plots (with or without sparsity maximization) is observed in the latest stages of training. As the artifacts are removed by enhancing the sparsity of the heatmaps, the detection performance at the pixel level increases for every lesion type. We hypothesized that maximizing the sparsity of the heatmaps would also speed up the training process, by reducing the search space. However, we did not observe such a behavior.

Performance at the image level is also very high, which was to be expected since we reused an efficient ConvNet from a recent machine learning competition: a performance of $A_z = 0.954$ was achieved by the proposed framework in Kaggle-test, as opposed to $A_z = 0.946$ for the system by Colas et al. (2016). Based on the above observations at the pixel level, we derived a novel ensemble of ConvNets that outperforms our main baseline solution, namely o_O: a performance of $A_z = 0.951$ was measured for the original o_O solution, as opposed to $A_z = 0.954$ for the proposed solution.

In this study, we focused on detecting referable DR for several reasons. First, this is the most useful classification in the context of DR screening: it determines whether or not the patient needs to be seen in person by an ophthalmologist. Second, the manual segmentations used to evaluate performance at the pixel level do not contain the most advanced signs of DR, such as neovascularizations, so additional manual segmentations would be needed for a relevant evaluation. Third, it allows comparison with the state of the art (Colas et al., 2016). However, unlike most multiple-instance learning algorithms, the proposed solution is not restricted to binary decision problems. The proposed solution is also general in the sense that it could be applied advantageously to all problems governed by a very limited number of relevant pixels. This class of problems was traditionally solved by multiple-instance Learning algorithms, but the proposed solution allows these problems to be solved by ConvNets as well, with enhanced performance. Finally, because the proposed framework is trained to detect relevant patterns in images using image-level labels only for supervision, it is able to discover new biomarkers in images. In that sense, it can be regarded as a general image mining tool, hence the paper’s title.

In conclusion, a general framework was proposed for solving multiple-instance problems with ConvNets and the relevance of this framework was demonstrated in the context of diabetic retinopathy screening.

9. Acknowledgements

This work was supported in part by a grant from the French *Fond Unique Interministériel* (FUI-19 RetinOpTIC). The authors would also like to thank the organizers and competitors

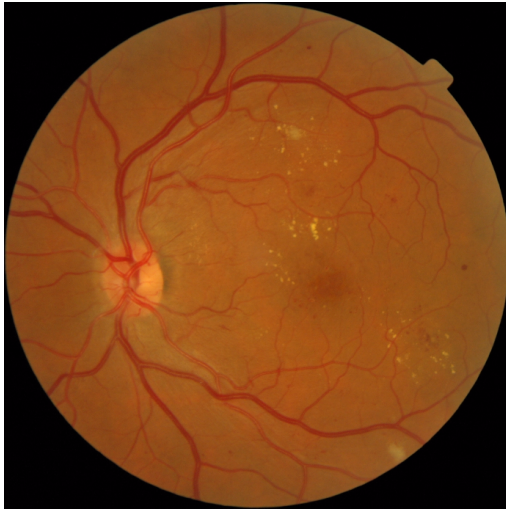
⁹<http://www.adcis.net/en/Download-Third-Party/Messidor.html>

of the Kaggle Diabetic Retinopathy competition for providing very useful data and ideas.

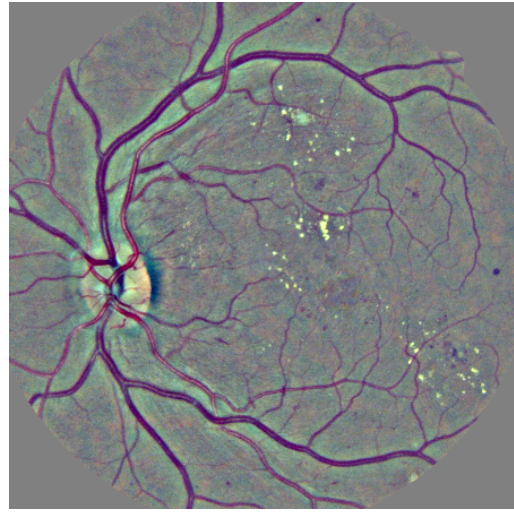
References

- Abràmoff, M. D., Garvin, M. K., Sonka, M., 2010. Retinal imaging and image analysis. *IEEE Rev Biomed Eng* 3, 169–208.
- Amores, J., Aug. 2013. Multiple instance classification: review, taxonomy and comparative study. *Artif Intell* 201, 81–105.
- Arunkumar, R., Karthigaikumar, P., 2016. Multi-retinal disease classification by reduced deep learning features. *Neural Comput Appl* (in press).
- Bach, S., Binder, A., Montavon, G., Klauschen, F., Müller, K.-R., Samek, W., Jul. 2015. On pixel-wise explanations for non-linear classifier decisions by layer-wise relevance propagation. *PLoS One* 10 (7).
- Barriga, E. S., McGrew, E., VanNess, R., Zamora, G., Nemeth, S. C., Bauman, W., Soliz, P., Apr. 2014. Assessing agreement between dilated indirect stereoscopic exam and digital non-mydiatic retinal photography for the evaluation of diabetic retinopathy. In: *Proc ARVO*. Vol. 55. Orlando, FL, USA, pp. 5335–5335.
- Bharali, P., Medhi, J., Nirmala, S., 2015. Detection of hemorrhages in diabetic retinopathy analysis using color fundus images. In: *Proc IEEE ReTIS*. Kolkata, India, pp. 237–242.
- Burlina, P., Freund, D., Joshi, N., Wolfson, Y., Bressler, N., Apr. 2016. Detection of age-related macular degeneration via deep learning. In: *Proc ISBI*. Prague, Czech Republic, pp. 184–188.
- Chen, X., Xu, Y., Wong, D., Wong, T., Liu, J., Aug. 2015a. Glaucoma detection based on deep convolutional neural network. In: *Proc IEEE EMBC*. Milan, Italy, pp. 715–718.
- Chen, X., Xu, Y., Yan, S., Wong, D., Wong, T., Liu, J., Oct. 2015b. Automatic feature learning for glaucoma detection based on deep learning. In: *Proc MICCAI*. Munich, Germany, pp. 669–677.
- Colas, E., Besse, A., Orgogozo, A., Schmauch, B., Meric, N., Besse, E., Oct. 2016. Deep learning approach for diabetic retinopathy screening. In: *Proc EVER*. Nice, France.
- Cuadros, J., Bresnick, G., May 2009. EyePACS: an adaptable telemedicine system for diabetic retinopathy screening. *J Diabetes Sci Technol* 3 (3), 509–516.
- Dai, B., Bu, W., Wang, K., Wu, X., 2016. Fundus lesion detection based on visual attention model. *Commun Comput Inform Sci* 623, 384–394.
- Franklin, S., Rajan, S., 2014. Diagnosis of diabetic retinopathy by employing image processing technique to detect exudates in retinal images. *IET Image Process* 8 (10), 601–609.
- Girshick, R., Donahue, J., Darrell, T., Malik, J., 2014. Rich feature hierarchies for accurate object detection and semantic segmentation. In: *Proc IEEE CVPR*. Washington, DC, USA, pp. 580–587.
- Goodfellow, I. J., Warde-Farley, D., Mirza, M., Courville, A., Bengio, Y., Jun. 2013. Maxout networks. In: *Proc ICML*. Vol. 28. Atlanta, GA, USA, pp. 1319–1327.
- Graham, B., Dec. 2014. Fractional max-pooling. *Tech. Rep. arXiv:1412.6071 [cs]*.
- Haloi, M., May 2015. Improved microaneurysm detection using deep neural networks. *Tech. Rep. arXiv:1505.04424 [cs]*.
- He, K., Zhang, X., Ren, S., Sun, J., Feb. 2015. Delving deep into rectifiers: surpassing human-level performance on ImageNet classification. *Tech. Rep. arXiv:1502.01852 [cs.CV]*.
- Hinton, G. E., Srivastava, N., Krizhevsky, A., Sutskever, I., Salakhutdinov, R. R., Jul. 2012. Improving neural networks by preventing co-adaptation of feature detectors. *Tech. Rep. arXiv:1207.0580 [cs]*.
- Kauppi, T., Kalesnykiene, V., Kamarainen, J.-K., Lensu, L., Sorri, I., Raninen, A., Voutilainen, R., Pietilä, J., Kälviäinen, H., Uusitalo, H., 2007. The DIARETDB1 diabetic retinopathy database and evaluation protocol. In: *Proc BMVC*. Warwick, UK.
- Kingma, D., Ba, J., May 2015. Adam: a method for stochastic optimization. In: *Proc ICLR*. San Diego, CA, USA.
- Kumar, P., Kumar, R., Sathar, A., Sahasranamam, V., 2014. Automatic detection of red lesions in digital color retinal images. In: *Proc IC3I*. Mysore, India, pp. 1148–1153.
- LeCun, Y., Bengio, Y., Hinton, G., May 2015. Deep learning. *Nature* 521 (7553), 436–444.
- Li, Q., Feng, B., Xie, L., Liang, P., Zhang, H., Wang, T., Jan. 2016. A cross-modality learning approach for vessel segmentation in retinal images. *IEEE Trans Med Imaging* 35 (1), 109–118.
- Lim, G., Cheng, Y., Hsu, W., Lee, M., Nov. 2015. Integrated optic disc and cup segmentation with deep learning. In: *Proc ICTAI*. Vietri sul Mare, Italy, pp. 162–169.
- Maji, D., Santara, A., Ghosh, S., Sheet, D., Mitra, P., Aug. 2015. Deep neural network and random forest hybrid architecture for learning to detect retinal vessels in fundus images. In: *Proc IEEE EMBC*. Milan, Italy, pp. 3029–3032.
- Maji, D., Santara, A., Mitra, P., Sheet, D., Mar. 2016. Ensemble of deep convolutional neural networks for learning to detect retinal vessels in fundus images. *Tech. Rep. arXiv:1603.04833 [cs, stat]*.
- Mane, V., Kawadiwale, R., Jadhav, D., 2015. Detection of red lesions in diabetic retinopathy affected fundus images. In: *Proc IEEE IACC*. Bangalore, India, pp. 56–60.
- Melendez, J., van Ginneken, B., Maduskar, P., Philipsen, R. H. H. M., Reither, K., Breuninger, M., Adetifa, I. M. O., Maane, R., Ayles, H., Sánchez, C. I., Jan. 2015. A novel multiple-instance learning-based approach to computer-aided detection of tuberculosis on chest X-rays. *IEEE Trans Med Imaging* 34 (1), 179–192.
- Nesterov, Y., 1983. A method of solving a convex programming problem with convergence rate $O(1/\sqrt{k})$. *Soviet Math Doklady* 27, 372–376.
- Nielsen, M. A., 2015. How the backpropagation algorithm works. In: *Neural networks and deep learning*. Determination Press, Ch. 2.
- Prentas, P., Loncaric, S., Sep. 2015. Detection of exudates in fundus photographs using convolutional neural networks. In: *Proc ISPA*. Zabreb, Croatia, pp. 188–192.
- Quelleg, G., Bazin, L., Cazuguel, G., Delafay, I., Cochener, B., Lamard, M., Apr. 2016a. Suitability of a low-cost, handheld, nonmydiatic retinograph for diabetic retinopathy diagnosis. *Transl Vis Sci Technol* 5 (2), 16.
- Quelleg, G., Lamard, M., Abràmoff, M. D., Decencière, E., Lay, B., Erginay, A., Cochener, B., Cazuguel, G., Aug. 2012a. A multiple-instance learning framework for diabetic retinopathy screening. *Med Image Anal* 16 (6), 1228–1240.
- Quelleg, G., Lamard, M., Cazuguel, G., Cochener, B., Roux, C., Jan. 2010a. Adaptive nonseparable wavelet transform via lifting and its application to content-based image retrieval. *IEEE Trans Image Process* 19 (1), 25–35.
- Quelleg, G., Lamard, M., Cazuguel, G., Cochener, B., Roux, C., Apr. 2010b. Wavelet optimization for content-based image retrieval in medical databases. *Med Image Anal* 14 (2), 227–241.
- Quelleg, G., Lamard, M., Cazuguel, G., Cochener, B., Roux, C., Apr. 2012b. Fast wavelet-based image characterization for highly adaptive image retrieval. *IEEE Trans Image Process* 21 (4), 1613–1623.
- Quelleg, G., Lamard, M., Cozic, M., Coatrieux, G., Cazuguel, G., Jul. 2016b. Multiple-instance learning for anomaly detection in digital mammography. *IEEE Trans Med Imaging* 35 (7), 1604–1614.
- Quelleg, G., Lamard, M., Erginay, A., Chabouis, A., Massin, P., Cochener, B., Cazuguel, G., Apr. 2016c. Automatic detection of referral patients due to retinal pathologies through data mining. *Med Image Anal* 29, 47–64.
- Russakovsky, O., Deng, J., Su, H., Krause, J., Satheesh, S., Ma, S., Huang, Z., Karpathy, A., Khosla, A., Bernstein, M., Berg, A. C., Fei-Fei, L., Apr. 2015. ImageNet large scale visual recognition challenge. *Int J Comput Vis* 115 (3), 211–252.
- Samek, W., Binder, A., Montavon, G., Lapuschkin, S., Müller, K. R., 2016. Evaluating the visualization of what a deep neural network has learned. *IEEE Trans Neural Netw Learn Syst* (in press).
- Simonyan, K., Vedaldi, A., Zisserman, A., Apr. 2014. Deep inside convolutional networks: visualising image classification models and saliency maps. In: *ICLR Workshop*. Calgary, Canada.
- Srivastava, R., Cheng, J., Wong, D., Liu, J., Apr. 2015. Using deep learning for robustness to parapapillary atrophy in optic disc segmentation. In: *Proc ISBI*. New York, NY, USA, pp. 768–771.
- Tibshirani, R., 1996. Regression shrinkage and selection via the lasso. *J Royal Statist Soc B* 58 (1), 267–288.
- Wilkinson, C. P., Ferris, F. L., Klein, R. E., Lee, P. P., Agardh, C. D., Davis, M., Dills, D., Kampik, A., Pararajasegaram, R., Verdager, J. T., Sep. 2003. Proposed international clinical diabetic retinopathy and diabetic macular edema disease severity scales. *Ophthalmology* 110 (9), 1677–1682.
- Winder, R. J., Morrow, P. J., McRitchie, I. N., Bailie, J. R., Hart, P. M., Dec. 2009. Algorithms for digital image processing in diabetic retinopathy. *Com-*

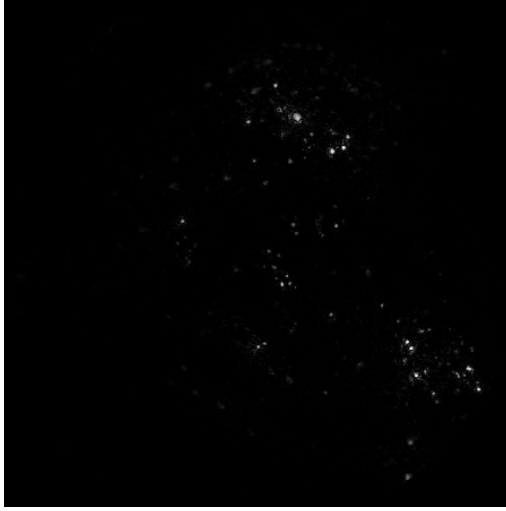
- put Med Imaging Graph 33 (8), 608–622.
- Yang, N., Lu, H.-C., Fang, G.-L., Yang, G., 2013. An effective framework for automatic segmentation of hard exudates in fundus images. *J Circuit Syst Comp* 22 (1).
- Yosinski, J., Clune, J., Nguyen, A., Fuchs, T., Lipson, H., Jul. 2015. Understanding neural networks through deep visualization. In: *Proc ICML DL Works*. Lille, France.
- Zeiler, M. D., Fergus, R., Sep. 2014. Visualizing and understanding convolutional networks. In: *Proc ECCV*. Zurich, Switzerland, pp. 818–833.



(a) original image



(b) preprocessed image



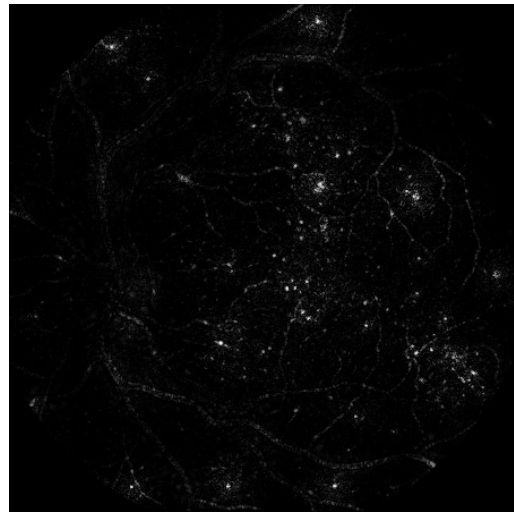
(c) π_{HE} — mostly bright lesions



(d) π_{RDR} — mostly red lesions



(e) $\bar{\pi}$ — all lesions

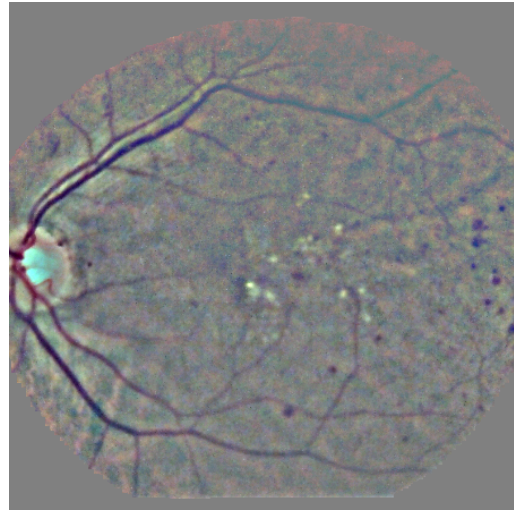


(f) π_0 — all lesions, but also blood vessels

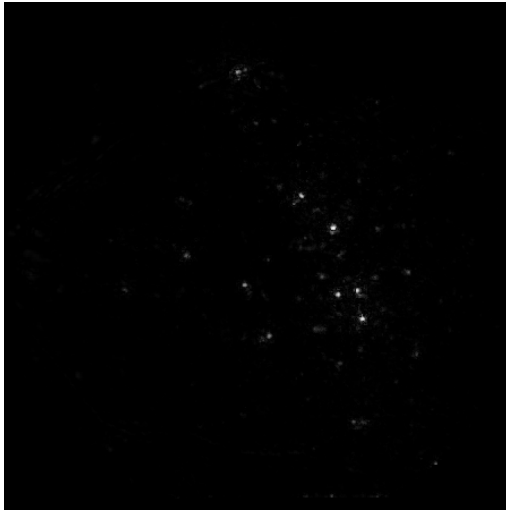
Figure 7: Examples of heatmaps from a fundus image of typical quality (image 20051020_57622_0100_PP.png from Messidor). π_0 was obtained without sparsity enhancement. π_{HE} and π_{RDR} were obtained with sparsity enhancement, using networks \mathcal{N}_{HE} and \mathcal{N}_{RDR} , respectively. $\bar{\pi}$ was obtained by averaging six π maps (including π_{HE} and π_{RDR}), where each π map is weighted according to the network's importance in the random forest.



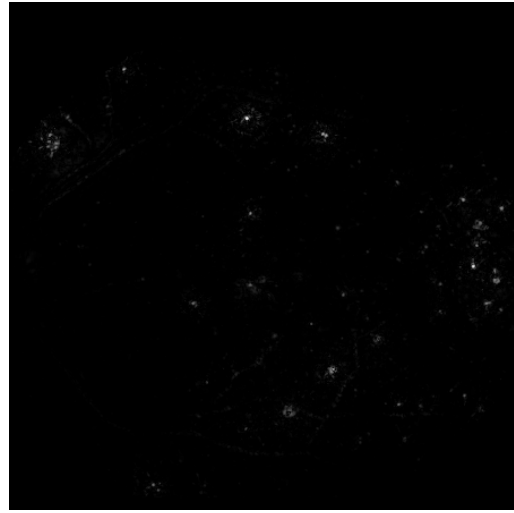
(a) original image



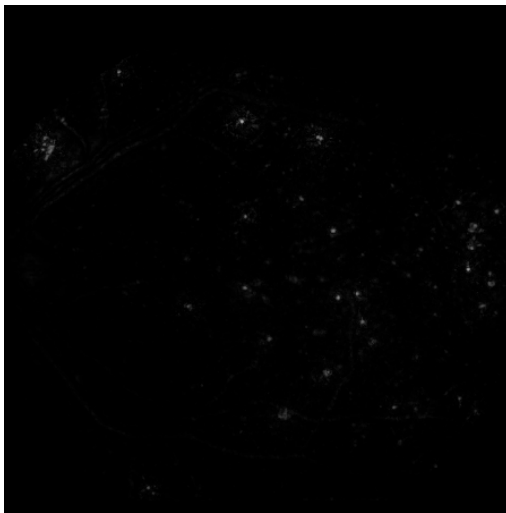
(b) preprocessed image



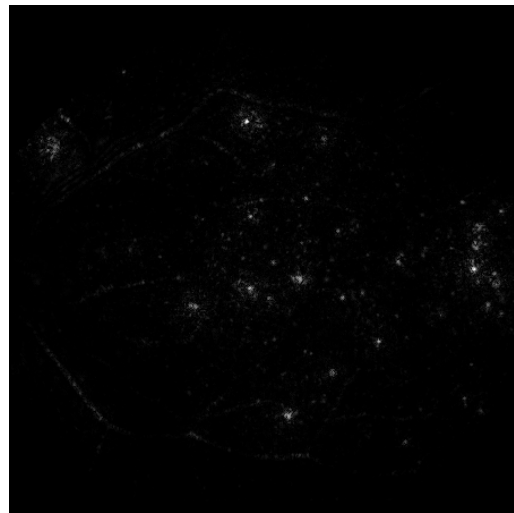
(c) π_{HE} — mostly bright lesions



(d) π_{RDR} — mostly red lesions



(e) $\bar{\pi}$ — all lesions



(f) π_0 — all lesions, but also blood vessels

Figure 8: Examples of heatmaps from a fundus image acquired with a low-cost handheld retinograph: the Horus DEC 200 (MiiS, Hsinchu, Taiwan). This image was acquired at Brest University Hospital in 2015 (Quellec et al., 2016a).